ACS OMEGA

Open Access

http://pubs.acs.org/journal/acsodf

Article

Novel Anion-Doped Cathode Material $SrFe_{1-x}Si_xO_{3-\delta}F_y$ for Intermediate-Temperature Solid Oxide Fuel Cells

Huipu Ma, Songbo Li,* Shengli An, Mengxin Li, Runze Sun, and Qiming Guo

Cite This: *ACS Omega* 2024, 9, 24633−24642

Read Online

ACCESS | Metrics & More | Article Recommendations | Supporting Information

ABSTRACT: $SrFe_{1-x}Si_xO_{3-\delta}F_y$ cathode materials (x = 0.05, 0.1, 0.15; y = 0, 0.1, 0.5) were prepared via a solid-state method. X-ray diffraction results show that the synthesized F doping samples were perovskite structure. X-ray photoelectron spectroscopy findings show that F^- anions were doped into $SrFe_{1-x}Si_xO_{3-\delta}$. Transmission electron microscopy and energy-dispersive spectroscopy were performed to analyze the microstructure and element distribution in the materials, respectively. Double-layer composite cathode symmetric cells were prepared through a screen printing method. Scanning electron microscopy images revealed that the double-layer composite cathode adhered well to the electrolyte. The doping with F^- can increase the coefficient of thermal expansion of $SrFe_{1-x}Si_xO_{3-\delta}$. The electrochemical impedance spectroscopy results indicate that the oxygen transport capacity of the $SrFe_{0.95}Si_{0.05}O_{3-\delta}$ material can be improved by doping with F^-, but such a method can decrease the oxygen transport capacity of $SrFe_{0.9}Si_{0.1}O_{3-\delta}$. At 800 °C, the peak power density of the single cell supported by an anode and $SrFe_{0.9}Si_{0.1}O_{3-\delta}F_{0.1}$ as the cathode reached 388.91 mW/cm^2. Thus, the incorporation of F^- into $SrFe_{1-x}Si_xO_{3-\delta}$ cathode materials can improve their electrochemical performance and enable their application as cathode materials for solid-oxide fuel cells.

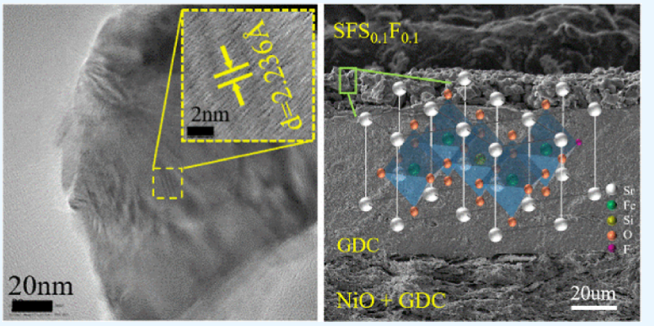

1. INTRODUCTION

Given the characteristics of environmental protection, safety, and high energy efficiency, solid oxide fuel cells (SOFCs) have become one of the development directions of future energy.[1] However, problems related to material properties, manufacturing processes, and production costs have slowed the commercialization of SOFCs. The problems associated with the development of SOFCs relate to operations at a high-temperature environment of 800−1000 °C. While operating at high temperature can improve the energy efficiency of SOFCs, it also results in a short lifetime and high maintenance costs.[2] Reduction of the operating temperature can improve the thermodynamic efficiency, expand the selection range of materials, reduce costs, and extend the lifespan of SOFCs. However, with the decrease in operating temperature, the electrochemical reaction kinetics of the cathode extremely slow down. Therefore, the development of novel low-temperature (600−800 °C) cathode materials is the key to developing SOFCs.

Oxides with mixed ion−electron conductivity exhibit good stability and high catalytic activity for the oxygen reduction reaction (ORR) and have attracted considerable research attention. As for mixed ionic−electronic conductor materials, perovskite oxides usually exhibit a cubic crystal configuration with the molecular formula $ABO_{3-\delta}$ (δ indicates oxygen vacancy). Mixed electron−ion conductive perovskite oxides have excellent chemical and structural stability and have been used in high-temperature electrochemical devices such as SOFCs, solid oxide electrolytes, and oxygen permeable membranes, showing application prospects in the field of energy conversion, utilization, and storage. $La_{1-x}Sr_xCo_{1-y}Fe_yO_3$, $Ba_{1-x}Sr_xCo_{0.8}Fe_{0.2}O_{3-\delta}$, and $Sm_{1-x}Sr_xCoO_{3-\delta}$,$SrFeO_{3+\delta}$ are used as SOFC cathode materials.[3] Perovskite oxides possess a chemical composition with a wide adjustable range. Appropriate doping can enhance the ionic conductivity to improve the performance of fuel cell devices.[4] Combining α-Fe_2O_3 with carbon materials with good electrical conductivity (such as carbon nanosheets, carbon nanotubes, and graphene nanosheets) can increase the conductivity of α-Fe_2O_3 and improve its electrochemical performance.[5] The electrochemical properties of $Li_4Mo_5O_{17}$ are improved by the MoO_6 oxyanion.[6] Researchers regulate the phase structure of perovskite oxides through element doping, which improves the catalytic activity of ORR and coefficient of thermal expansion (CTE).[7] The change of the valence state of B-site elements and the oxygen vacancy caused by doping

Received: January 31, 2024
Revised: April 26, 2024
Accepted: May 8, 2024
Published: May 24, 2024

elements will affect the mixed conductivity of the perovskite. In addition to transition metal elements, nonmetallic elements Si can also partially replace the B-position. The apatite structure of oxygen ion conductor $Ln_{10}(SiO_4)_6O_3$ (Ln = La, Nd, Sm, Gd, and Dy) can be used as the electrolyte material of SOFC. The conductivity of the above materials can reach 2.3×10^{-4} S/cm at 500 °C. The ionic conductivity of Sr(Si, Ge)O_3 doped with Na/K at 625 °C is 1×10^{-2} S cm^{-2}.[8] Merkulov et al. studied the crystal structure of $SrFe_{1-x}Si_xO_{3-\delta}$ and analyzed the effects of Si doping on the valence state of Fe and O vacancies.[9] The perovskite $SrFe_{1-x}Si_xO_{3-\delta}$ ($x \leq 0.15$) was synthesized under ordinary pressure via a solid-state method.[10] The stability after the reduction reaction, conductivity, and area specific resistance (ASR) of $SrFe_{1-x}Si_xO_{3-\delta}$ were tested. SiO_2 is a widely recognized harmful pollutant that degrades the properties of SOFC electrolyte materials, which results in a high grain-boundary resistance.[11] However, the substitution of Si^{4+} with Fe has a positive influence on the structural stability and electrochemical properties of the iron-based perovskite $SrFe_{1-x}Si_xO_{3-\delta}$. The doping of Si inhibits the suppression of perovskite → brownmillerite transition in $SrFeO_{3-\delta}$, which is conducive to vacancy order in the low-temperature range (450−600 °C). The $SrFe_{0.9}Si_{3-\delta}$ material has the ASR of $SrFe_{0.9}Si_{0.1}O_{3-\delta}$ of 0.08 Ω·cm^2 at 800 °C. Its conductivity peaks at 400 °C and decreases with increasing temperature. At 800 °C, the conductivity of the $SrFe_{0.9}Si_{0.1}O_{3-\delta}$ material decreases to 24.1 S/cm, which does not meet the basic requirement of cathode material conductivity ≥100 S/cm. Therefore, $SrFe_{1-x}SixO_{3-\delta}$ can be used as a new low-temperature cathode material.

As for the improvement of the properties of SOFC cathode materials, doping cations with different radii or valences to partially replace A or B sites can increase the oxygen vacancy concentration and improve surface reaction kinetics, but the process will lead to the transformation of the cubic symmetric configuration of perovskite, which is disadvantageous for its catalytic activity at low temperatures.[12] Therefore, the partial replacement of oxygen ions of perovskite oxides with anions, such as Cl^-,[13] F^-,[14] N^{3-},[15] or S^{2-},[16] can be considered to improve the interfacial reactivity of perovskite oxides. If S is introduced into the $Li_4Ti_5O_{12}$ electrode material, the electrochemical performance can be improved environmentally and at low cost.[17] $Sr_2Fe_{1.5}Mo_{0.5}O_{5.8}Cl_{0.2}$ still maintains the cubic structure of $Fm\bar{3}m$ and reduces the ASR value about 21% compared with $Sr_2Fe_{1.5}Mo_{0.5}O_6$.[18] The high electronegativity of F can reduce the valence electron density of oxygen, weakening the chemical bond between A/B cations and oxygen. The partial replacement of the ion with the asymmetrical oxidation of O^{2-} by the F^- ion can improve the electrochemical performance of $SrFe_{1.5}Mo_{0.5}O_{2.9}F_{0.1}$. The ionic radius of F^- is close to that of the ring of O^{2-}, and doping does not affect the cubic structure of $Sr_2Fe_{1.5}Mo_{0.5}O_6$. Meanwhile, F has a higher electronegativity and a lower valence electron density; therefore, doping F can weaken the M−O bond in $Sr_2Fe_{1.5}Mo_{0.5}O_6$ and increase the activity of lattice oxygen. Some researchers added F to the Co-based perovskite oxide $La_{0.6}Sr_{0.4}Co_{0.2}Fe_{0.8}O_{3-\delta}$, which enhanced its oxygen-transport performance and ORR activity.[19] The double perovskite oxide $LaBa_{0.5}Sr_{0.5}Fe_2O_{5.875-\delta}F_{0.125}$ cathode material has good electrochemical performance and electrode stability, and the assembled single cell has a power density that can reach 511 mW/cm.[2,20] $SrFeO_{3-\sigma-\delta}F_\sigma$ and $SrFe_{0.9}Ti_{0.1}O_{3-\sigma-\delta}F_\sigma$ cathode materials can improve the bulk phase diffusion and oxygen surface exchange properties.[21] In summary, doping anions at O sites can effectively improve the ORR activity of perovskite oxide materials.

In this paper, F was introduced into $SrFe_{1-x}Si_xO_{3-\delta}F_y$ (x = 0.05, 0.1, 0.15; y = 0, 0.1, 0.5) cathode materials, and the effects of anion doping on the structure and comprehensive electrochemical properties of the $SrFe_{1-x}Si_xO_{3-\delta}$ perovskite were studied in detail.

2. EXPERIMENTAL SECTION

2.1. Cathode Powder. $SrFe_{1-x}Si_xO_{3-\delta}F_y$ (x = 0.05, 0.1, 0.15; y = 0, 0.1, 0.5) cathode powder was prepared via a solid-state method. $SrCO_3$ (AR, 99%), SrF_2 (AR, 99%), Fe_2O_3 (AR, ≥99.0%), and SiO_2 (AR, 99%) were calculated and weighed at certain stoichiometric ratios. The reactants were ground and heated to 1000 °C in a Muffle furnace for 12 h. A planetary ball mill was used for ball milling (350 rpm) for 1 h, and the powder was heated to 1050 °C for 12 h. The powder was milled again for 1 h and then heated to 1100 °C for 12 h. The black powder was obtained as the target material. $SrFe_{1-x}Si_xO_{3-\delta}F_y$ was named as SFS_xF_y (x = 0.05, 0.1, 0.15; y = 0, 0.1, 0.5) based on the doping amount of Si and F.

2.2. Characterization. The phase structure of SFS_xF_y was determined by X-ray diffraction (XRD, Rigaku, MiniFlex 600). The atomic position and cell parameters were obtained through a Rietveld structure refinement. The target was CuKα (λ = 0.15418 nm), the scanning range was 10−80°, and the scanning rate was 4°/min. X-ray photoelectron spectroscopy (XPS, Thermo Scientific, EscaLab250Xi) was used to determine the properties of the elements in the obtained samples. Transmission electron microscopy (TEM, FEI, Tecnai F20) and energy-dispersive spectroscopy (EDS, Oxford, X-max20) were applied to analyze the high-resolution microstructure and element distribution of the materials, respectively. Ion chromatography (Thermo Fisher Scientific, Dionex Aquion) and potentiometric titration were used to analyze the F content in the samples. Field-emission scanning electron microscopy (SEM, Tescan, GAIA3) was conducted to observe the microscopic morphology of the symmetric cells. The CTE of the material was tested by using a thermal expansion analyzer (NETZSCH, DIL402C).

2.3. Electrical Performance Test. The black cathode material was milled for 1 h (350 rpm), pressed into strips at 200 MPa, and calcined at 1100 °C for 12 h. Then, its conductivity was measured via a four-electrode method.

The $Gd_{0.20}Ce_{0.80}O_{1.90}$ (GDC) electrolyte was prepared via a sol−gel method and calcined at 1250 °C for 10 h after pressing at 200 MPa. A symmetric cell with a double-layer composite cathode was prepared in the experiment.[22] The preparation of the first layer of the composite cathode slurry is as follows: The cathode powder and electrolyte were weighed at the mass ratio of 1:1, mixed with terpineol and ethyl cellulose at a certain proportion, and ground evenly. The composite cathode paste was coated on both sides of the GDC electrolyte through a screen printing method. After drying in an infrared oven, the second layer of the cathode paste was obtained by mixing the cathode powder with terpinol and ethyl cellulose in proportions. After drying, the composite cathode was calcined at 1100 °C for 10 h, and silver pulp and silver wire were used as the collector layer and reference electrode, respectively. Thus, a symmetric cell with a double-layer composite cathode was obtained. Polarization impedance was tested in the

https://doi.org/10.1021/acsomega.4c00869
ACS Omega 2024, 9, 24633−24642

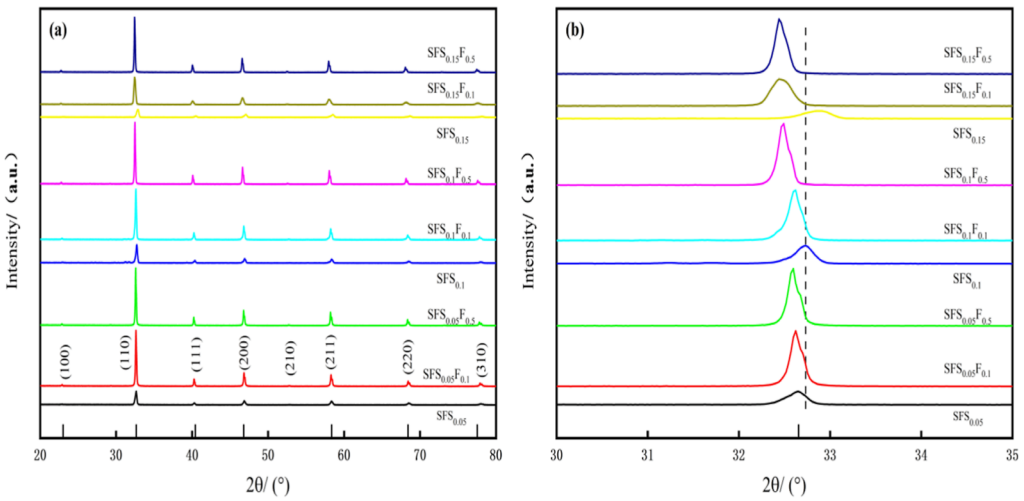

Figure 1. (a) XRD patterns of SFS_xF_y. (b) Local magnification diagram.

Table 1. Tolerance Factors (t) of SFS_xF_y

valence		$SFS_{0.05}$	$SFS_{0.05}F_{0.1}$	$SFS_{0.05}F_{0.5}$	$SFS_{0.1}$	$SFS_{0.1}F_{0.1}$	$SFS_{0.1}F_{0.5}$	$SFS_{0.15}$	$SFS_{0.15}F_{0.1}$	$SFS_{0.15}F_{0.5}$
Si^{4+}	Fe^{3+}	0.8817	0.8818	0.8822	0.8865	0.8866	0.8871	0.8914	0.8915	0.8920
Si^{4+}	Fe^{2+}	0.8348	0.8349	0.8352	0.8415	0.8416	0.8435	0.8483	0.8483	0.8487

Table 2. Cell Parameters of the Crystal Structure for $SrFe_{1-x}Si_xO_{3-\delta}F_y$

	$SrFe_{1-x}Si_xOF_y$								
Si (x)		0.05			0.1			0.15	
F (y)	0	0.1	0.5	0	0.1	0.5	0	0.1	0.5
α (Å)	3.865	3.870	3.874	3.873	3.874	3.882	3.878	3.883	3.887
c (Å)	3.865	3.870	3.874	3.873	3.874	3.882	3.878	3.883	3.887
V/(Å^3)	57.74	57.98	58.15	58.10	58.15	58.50	58.34	58.54	58.75

temperature range of 800−600 °C under an air atmosphere. The equivalent circuit was fitted by using Z-view software.

NiO and GDC were mixed at a mass ratio of 6:4, and the anode powder was obtained by ball milling for 10 h. The NiO-GDC/GDC/SFS_xF_y single cell was obtained by copressing NiO-GDC and GDC powder together at 200 MPa, calcined at 1250 °C for 10 h, coated with cathode powder via the screen printing method, and calcined at 1000 °C for 10 h. The anode used 30 mL/min wet hydrogen (3% H_2O) as fuel gas, and the cathode used static air as the oxidant. The power density of a single cell was tested by using an electrochemical workstation (Metrohm, PGSTAT302N).

3. RESULTS AND DISCUSSION

Figure 1 shows the XRD patterns of SFS_xF_y (x = 0.05, 0.1, 0.15; y = 0, 0.1, 0.5) series materials. The diffraction peaks of all samples were consistent with the typical cubic perovskite structure of $SrFeO_{3-\delta}$ (JCPDS PDF#34-0638). The diffraction peaks of the samples doped with F all conform to the structure of $SrFeO_{3-\delta}$, showing a typical cubic perovskite structure. No impure phase was produced in the sample doped with F. F(136 pm) with a smaller ionic radius enters the oxygen lattice (140 pm), and the diffraction peak shifts to a lower angle. The displacement degree of the diffraction peak is higher with the increase of the F doping amount. The tolerance factor (t) of SFS_xF_y (Table 1) is close to 1, as shown in eq 1. This implies that the crystal structure gradually shifts toward symmetry as the F^- content increases, which is consistent with previous reports.[19]

The tolerance factor (t) of SFS_xF_y (Table S1) is close to 1, which is between 0.8348 and 0.8920, as shown in eq 1. This implies that the crystal structure gradually shifts toward symmetry as the F^- content in SFS_xF_y increases, consistent with previous reports.[19]

$$t = \frac{r_A + \frac{(3-x)r_O + xr_F}{3}}{\sqrt{2}\,r_B + \frac{(3-x)r_O + xr_F}{3}} \quad (1)$$

In formula 1, r_A, r_B, and r_O represent the radii of the cation, oxygen, and fluorine anion at the A and B positions, respectively. FullProf software was used to conduct the fine analysis of XRD data. The cubic phase model was used to fit the findings, and the value of fit factor was within the acceptable range. Table 2 shows that materials with a high F doping amount had large cell parameters. For the $SrFe_{1-x}Si_xO_{3-\delta}$ material, cell parameters increased with the increase in the Si content because of the corresponding reduction of Fe^{4+} and the increase of Fe^{3+} content with the doping of Si^{4+}. The results are consistent with ref 10.

The surface elements of $SFS_{0.1}F_{0.1}$ were analyzed through XPS to verify the inclusion of Si and F in the perovskite lattice of the sample. As shown in Figure 2a, Sr, Fe, Si, and F atoms in $SFS_{0.1}F_{0.1}$ were detected, and the atomic ratios of all elements were consistent with the theoretical values. As shown in Figure 2b, the characteristic spectrum of O 1s presented two peaks at 528.78 and 531.27 eV.[23] The peak with a lower binding energy was classified as lattice oxygen, and that with a higher binding

https://doi.org/10.1021/acsomega.4c00869
ACS Omega 2024, 9, 24633−24642

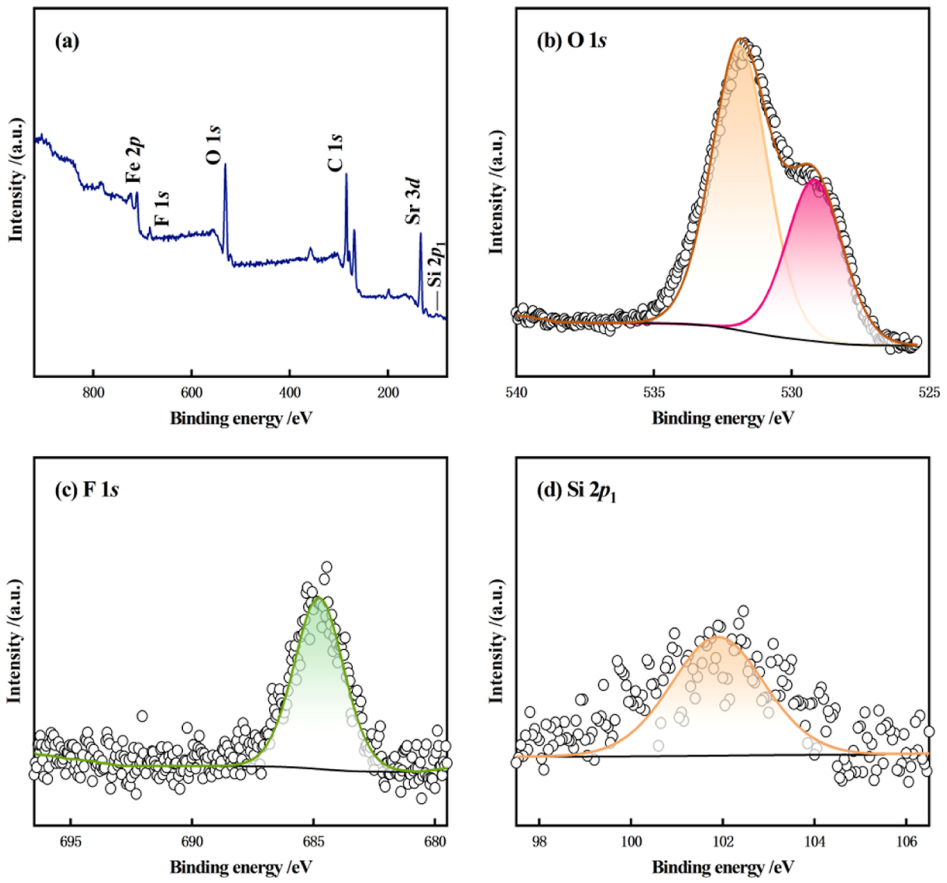

Figure 2. (a) XPS wide-scan spectrum of $SFS_{0.1}F_{0.1}$ powder; (b) O 1s; (c) F 1s; and (d) Si $2p_1$.

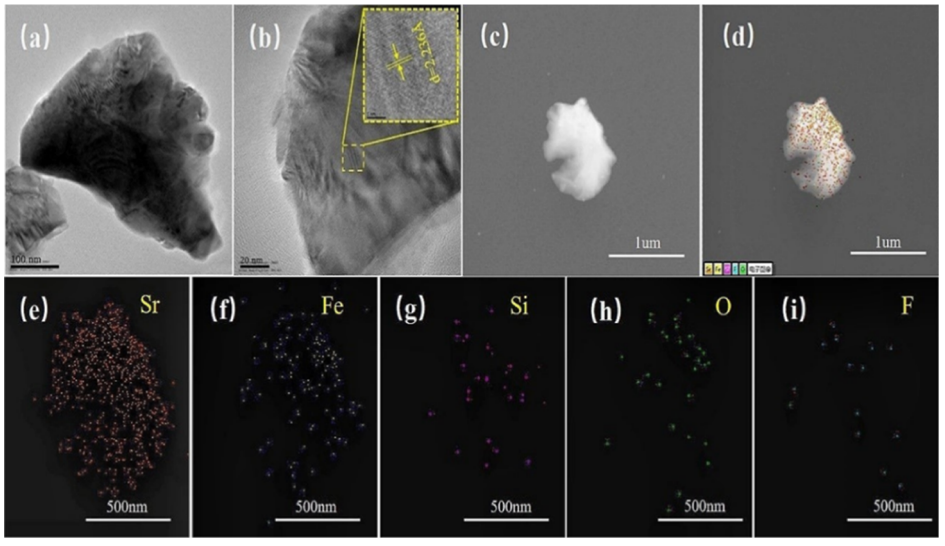

Figure 3. (a) TEM image of $SFS_{0.1}F_{0.1}$ powder; (b) HR-TEM image (enlarged view of the selected yellow area); (c) selected area electron diffraction image; (d) EDS image; and (e−i) element distribution.

energy was classified as adsorbed oxygen. The peak at the bond energy of 685 eV (Figure 2c) was classified as F 1s, which indicates that the valence state of F in $SFS_{0.1}F_{0.1}$ was −1.[19] In addition, the Si $2p_1$ peak was detected at 103.7 eV (Figure 2d), which brought electrons mainly from the single atoms of silicon. The reasons for the change in conductivity were analyzed in combination with XPS. XPS analyzes changes in the oxygen vacancy content and valence state changes of Fe, as shown in Tables S2 and S3. More oxygen vacancies and active sites for oxygen adsorption/dissociation can be obtained when the doping amount of F is 0.1. The introduction of excess F^- reduces the content of Fe^{2+}, which is not conducive to the electrochemical performance of the material.

To further characterize the crystal structure and microscopic morphology of the material, we used EDS and TEM to analyze the $SFS_{0.1}F_{0.1}$ single perovskite phase (Figure 3). Figure 3a

https://doi.org/10.1021/acsomega.4c00869
ACS Omega 2024, 9, 24633−24642

shows irregular particles with diameters between 100 and 200 nm. Figure 3b displays the local high-magnification transmission in the selected range of the yellow box, and the width of the diffraction fringe is 0.229 nm. It matched the lattice spacing of the (111) crystal face of the $SrFeO_{3-\delta}$ cubic structure, which is consistent with the XRD results. In addition, EDS images of $SFS_{0.1}F_{0.1}$ were collected to determine the element composition and distribution (Figure 3d). As shown in Figure S1, the proportion of Sr, Fe, and Si elements is basically close to the stoichiometric ratio of $SFS_{0.1}F_{0.1}$, while the proportion of the F element is low, as is shown in Table 3.

Table 3. EDS Data of the $SFS_{0.1}F_{0.1}$ and $SFS_{0.1}F_{0.5}$ Samples

		element			
sample	items	Sr	Fe	Si	F
$SFS_{0.1}F_{0.1}$	wt %	47.56	30.28	2.29	0.34
	At %	0.226	0.225	0.034	0.007
	elements ratio (EDS)	1.027	1.022	0.154	0.032
	elements ratio (formula)	1	0.9	0.1	0.1
$SFS_{0.1}F_{0.5}$	wt %	43.88	30.77	2.57	0.77
	At %	0.228	0.250	0.042	0.018
	elements ratio (EDS)	1.036	1.136	0.191	0.082
	elements ratio (formula)	1	0.9	0.1	0.5

It may be due to partial decomposition of strontium fluoride under high-temperature conditions. Figure 3e–i shows the element mappings of Sr, Fe, Si, and F. The element mappings of Sr and Fe clearly outline the shape of the $SFS_{0.1}F_{0.1}$ particles, while the element mappings of Si, O, and F also show similar shapes and distributions. All elements have no significant element aggregation or separation. It also reflects the evenly doping of F^- in the $SFS_{0.1}F_{0.1}$ lattice. The EDS test was carried out on the $SFS_{0.1}F_{0.5}$ sample, and the F content of the $SFS_{0.1}F_{0.5}$ sample was analyzed. As shown in Figure S2 and Table 3, the content of F in $SFS_{0.1}F_{0.5}$ is higher than that in $SFS_{0.1}F_{0.1}$, and the proportion of the F element in both is low.

The lines in Figure 4a,b are chromatograms of $SFS_{0.1}F_{0.5}$ and $SFS_{0.1}F_{0.1}$ standard solutions, respectively. It can be seen that the F^- ion in the sample is well separated, and the retention time is less than 7 min. The concentrations of the F^- ion in $SFS_{0.1}F_{0.5}$ and $SFS_{0.1}F_{0.1}$ samples are 4511.65 and 187.29 mg/L, respectively. The content of fluorine in the sample is determined by potentiometric titration by measuring the change of potential during titration. The 0.5 g sample was put into a conical bottle, and then 4 mL of 0.15 $mol{\cdot}L^{-1}HNO_3$ solution and 200 mL of deionized water were added in it with ultrasonic vibration for 60 min to dissolve the sample. Then, 10 mL of 1 $mol{\cdot}L^{-1}$ NaCl was subsequently added in it. Titration was carried out with a standard solution of $AgNO_3$, and the titration end point is the voltage abrupt point. The amount of the $AgNO_3$ solution consumed by titration subtracts the amount of Cl^-, and the difference value is the amount of F^-. The mass fractions of F^- in $SFS_{0.1}F_{0.5}$ and $SFS_{0.1}F_{0.1}$ samples are 0.63 and 0.19, respectively. The results of ion chromatography are consistent with those of potentiometric titration. Combined with the EDS results, it can be seen that the contents of F^- in $SFS_{0.1}F_{0.5}$ and $SFS_{0.1}F_{0.1}$ are lower than the stoichiometric ratio, and the content of F^- in $SFS_{0.1}F_{0.5}$ is higher than that in $SFS_{0.1}F_{0.1}$.

Figure 5 shows the SEM images of the cross-section of symmetrical cell $SFS_xF_y|SFS_xF_y$-GDC|GDC|SFS_xF_y-GDC|SFS_xF_y with a double-layer composite cathode. The images showed that the prepared double-layer composite cathode SFS_xF_y material attached well to the GDC electrolyte without delamination. The composite cathode was thin, and no evident boundary was observed in the SEM image. All the studied cathode materials had porous structures, which provided more active sites for gas diffusion from the cathode surface to the three-phase boundary, which is expected to have good ORR activity.[24] The cathode added with F exhibited a loose structure, which is conducive to ORR. When the doping

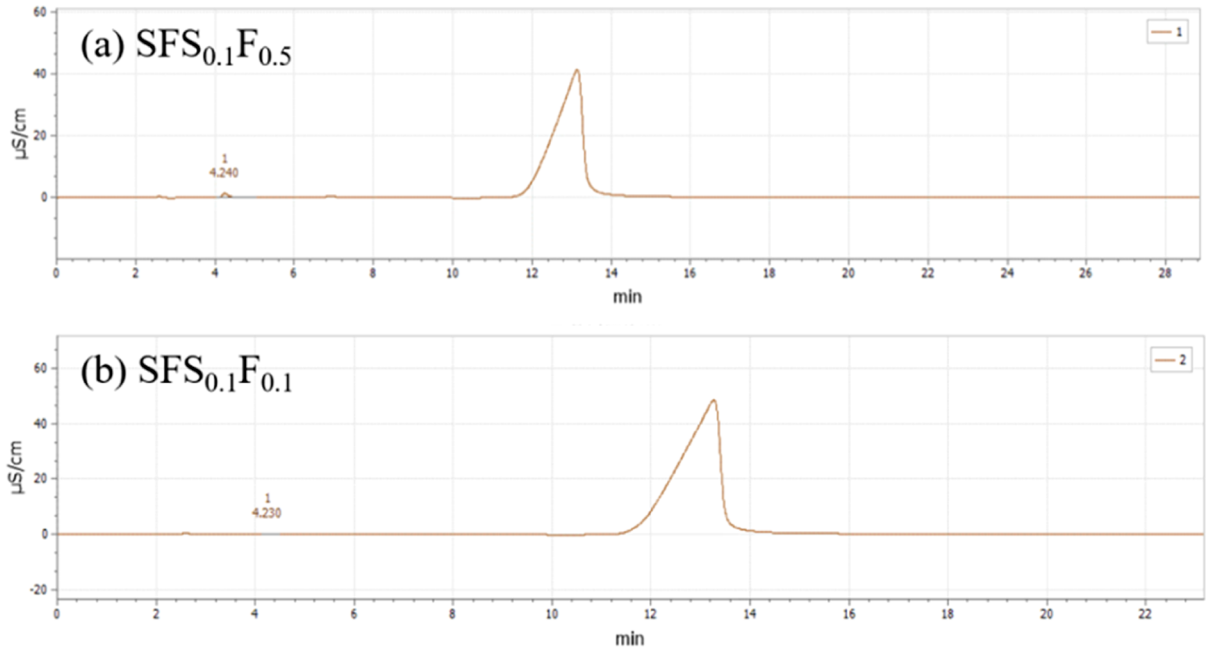

Figure 4. Chromatogram of the F^- ion.

https://doi.org/10.1021/acsomega.4c00869
ACS Omega 2024, 9, 24633−24642

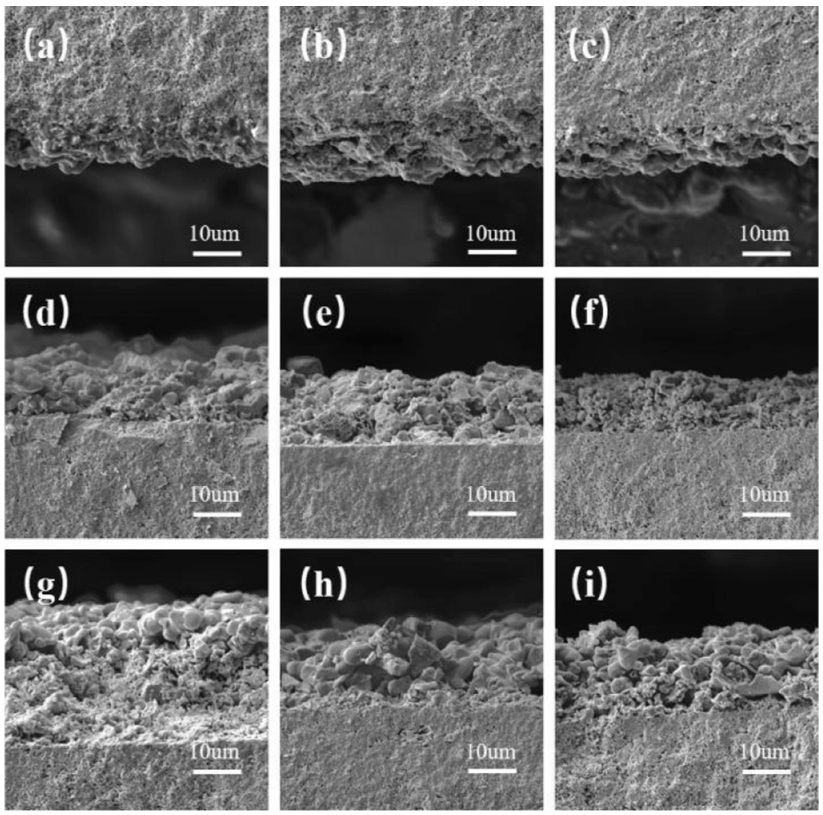

Figure 5. SEM images of the cell cross-section by SFS_xF_y as the cathode: (a) $SFS_{0.05}$, (b) $SFS_{0.1}$, (c) $SFS_{0.15}$, (d) $SFS_{0.05}F_{0.1}$, (e) $SFS_{0.1}F_{0.1}$, (f) $SFS_{0.15}F_{0.1}$, (g) $SFS_{0.05}F_{0.5}$, (h) $SFS_{0.1}F_{0.5}$, and (i) $SFS_{0.15}F_{0.5}$.

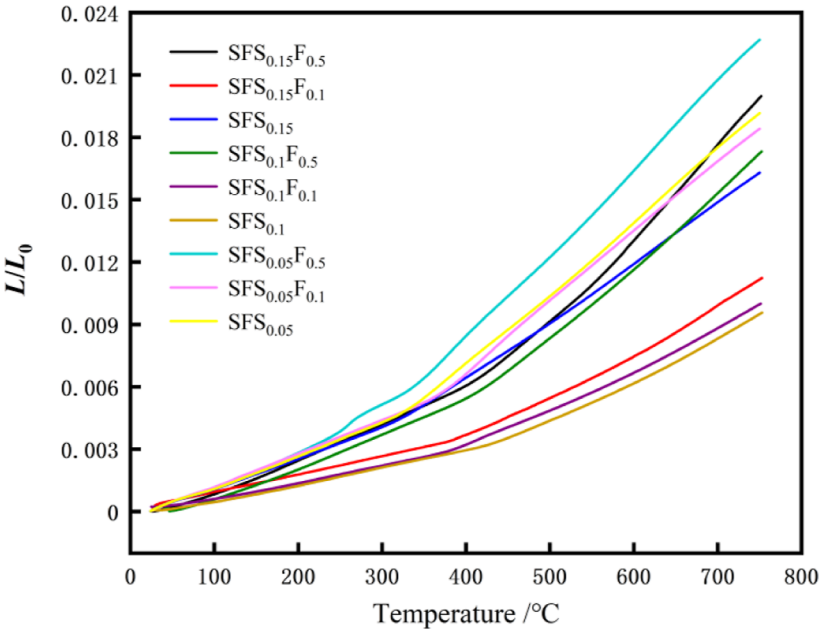

Figure 6. Relationship between the temperature and CTE of the SFS_xF_y samples.

amount of F was increased, agglomeration and coarsening occurred in $SFS_xF_{0.5}$ materials (Figure S3), aggregation and coarsening of samples may be due to crystal growth caused by F doping, and the pores were partially covered. This condition hindered the diffusion of gas and adversely affected the ORR activity.

Figure 6 shows the CTE curves of $SrFe_{0.9}Si_{0.1}O_{3-\delta}$ and $SrFe_{0.85}Si_{0.15}O_{3-\delta}$ doped with different F doping amounts. The figure also shows that the slope of each curve increased with an increase in temperature above 400 °C, which was due to the transformation of Fe^{4+} to Fe^{3+} during heating. Such a condition resulted in the escape of lattice oxygen and the formation of oxygen vacancies. The higher the doping amount of F, the steeper the CTE curve of the cathode material. The introduction of the F anion reduces the metal−oxygen bond energy, and oxygen is easy to overflow, thus increasing the

https://doi.org/10.1021/acsomega.4c00869
ACS Omega 2024, 9, 24633−24642

CTE of the material. CTE decreases with the increase in Si content, which is due to the reduction of the Fe content, the reduction of thermal reduction from Fe^{3+}, and the weakening of oxygen loss during heating. As shown in Table 4, the higher

Table 4. Average CTE Values of the SFS_xF_y Samples

sample	coefficient of thermal expansion (10^{-6} K^{-1})		
	30−400 °C	400−800 °C	30−800 °C
$SFS_{0.05}$	17.4096	34.9798	27.0169
$SFS_{0.05}F_{0.1}$	16.4760	33.6706	25.8610
$SFS_{0.05}F_{0.5}$	18.1150	41.4593	32.2748
$SFS_{0.1}$	7.9259	19.1053	11.9850
$SFS_{0.1}F_{0.1}$	7.7517	19.1999	12.5920
$SFS_{0.1}F_{0.5}$	15.6050	34.0809	24.1420
$SFS_{0.15}$	15.8455	28.7530	22.7391
$SFS_{0.15}F_{0.1}$	8.7752	21.4550	13.8341
$SFS_{0.15}F_{0.5}$	16.6123	40.5597	26.6837

the amount of F doping, the more evident the increase in average CTE. When the doping amount of F reached 0.5, the CTE of the $SFS_xF_{0.5}$ (x = 0.1, 0.15) material was higher than that of commonly used electrolytes (10−13 × 10^{-6} K^{-1}),[25] which easily caused cracking, deformation, and contact interface between the cathode and electrolyte materials.

Material conductivity was tested in an air atmosphere (Figure 7). The peak electrical conductivity of all materials

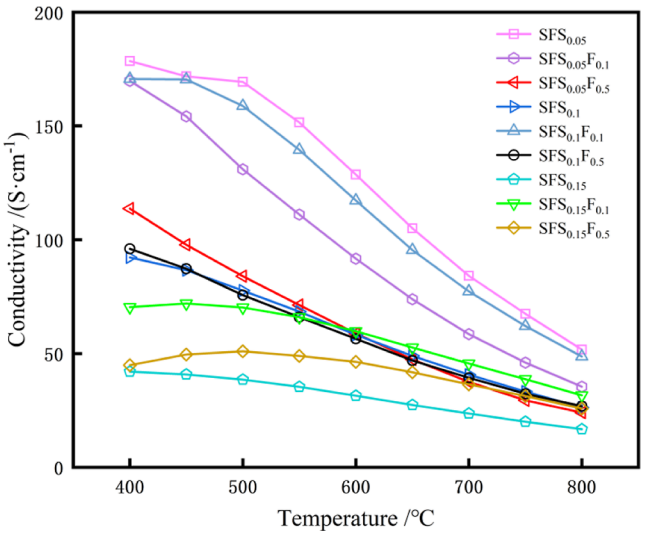

Figure 7. Conductivity−temperature curve of SFS_xF_y at 400−800 °C.

appeared at 400 °C and decreased with the increase in temperature due to the escape of lattice oxygen at high temperature and small polaron associated with the lower state of the silicon/iron.[26] Given the existence of randomly oriented nanocrystals in the $SrFe_{1-x}SixO_{3-\delta}$ perovskite matrix, the $SrFe_{0.95}Si_{0.05}O_{3-\delta}$ structure was the main perovskite phase ($Pm\bar{3}m$ space group), and the calcium ferrite structure $Sr_2(Fe_{1-x}Si_x)_2O_5$ coexisted.[9] The binding energy of metal−oxygen bonds was reduced due to the excellent capability of F to attract electrons.[27] Conductivity decreased with the increase in the doping amount of F. For $SFS_{0.1}F_y$ and $SFS_{0.15}F_y$ (y = 0, 0.1, 0.15) series materials, the doping of F improved their conductivity because the introduced F expanded the lattice volume, generated oxygen vacancies, and improved ionic conductivity. More oxygen vacancies and active sites for oxygen adsorption/dissociation can be obtained when the doping amount of F is 0.1. The introduction of excess F^- reduces the content of Fe^{2+}, which is not conducive to the electrochemical performance of the material.

To evaluate the effect of F^- doping on the ORR activity of the cathode materials, we assembled a symmetric cell with a double-layer composite cathode structure. Figure 8 shows the impedance spectra of SFS_xF_y at the temperature range of 600−800 °C. The equivalent circuit L-R_s-(R_1-CPE_1)-(R_2-was) is used to fit the AC impedance spectrum. The presence of two arcs in the impedance spectrum indicates that two electrode processes were involved in molecular oxygen reduction. The high-frequency arc was caused by polarization in the charge transfer process, and the low-frequency arc was due to oxygen adsorption and desorption on the electrode surface related to cation diffusion. As shown in the equivalent circuit diagram, R_1 refers to the charge transfer resistance caused by the electrochemical reaction at the electrode−electrolyte interface, and R_2 denotes the diffusion resistance caused by the diffusion of oxygen ions at the electrode. The polarization impedance R_p consists of the charge transfer impedance R_1 at high frequencies and the diffusion impedance R_2 at low frequencies. R_1, R_2, and R_p values of the cathode materials at 800 °C are shown in Figure 9. On the one hand, the appropriate substitution of F anions for oxygen ions can improve the activity of the $SFS_{0.05}F_y$ material because F ions have a higher electronegativity than oxygen ions, and the ORR activity can be improved by doping F. The polarization impedance values of $SFS_{0.1}F_y$ and $SFS_{0.15}F_y$ materials increased because the introduction of F increased the concentration polarization, hindered the self-diffusion of oxygen, and reduced the diffusion rate of oxygen ions. The increase of the polarization impedance values of $SFS_{0.1}F_y$ and $SFS_{0.15}F_y$ materials is mainly due to the increase of the diffusion impedance R_2, as shown in Figure 9, which is related to the increase of the concentration polarization, as is shown in Figure 8.

Figure 10 displays the cross-sectional morphology of a single cell with NiO-GDC as the anode, $SFS_{0.1}$ and $SFS_{0.1}F_{0.1}$ as the cathode, and GDC as the electrolyte. The electrolyte showed no evidently closed pores or penetrating holes, which can effectively isolate the gas between the cathode and anode. The NiO-GDC electrode had a porous structure and can efficiently transport gas and charge.

Figure 11 reveals the volt−ampere characteristics and output power curves of NiO-GDC/GDC/$SFS_{0.1}$ and NiO-GDC/GDC/$SFS_{0.1}F_{0.1}$ single cells at the temperature range of 800−650 °C, respectively. At 750 and 800 °C, the maximum power densities were 58.13 and 131.88 mW/cm^2, respectively. The $SFS_{0.1}F_{0.1}$ cathode cells attained maximum power densities of 278.86 and 388.91 mW/cm^2 at 750 and 800 °C, respectively, which imply an improved electrochemical performance. The polarization impedance of the $SFS_{0.1}F_{0.1}$ cathode material was as low as 0.244 Ω·cm^2 at 800 °C, which indicates that SOFCs with the $SFS_{0.1}F_{0.1}$ cathode material can operate at such temperature. The performance of a single cell is close to that of the relevant $SrFeO_{3-\delta}$-based cathode materials that have been reported, as shown in Table 5.

4. CONCLUSIONS

$SrFe_{1-x}Si_xO_{3-\delta}F_y$ (x = 0.05, 0.1, 0.15; y = 0, 0.1, 0.5) series cathode materials were synthesized via a solid-state method. The crystal structure was not changed by F doping. The cell

https://doi.org/10.1021/acsomega.4c00869
ACS Omega 2024, 9, 24633−24642

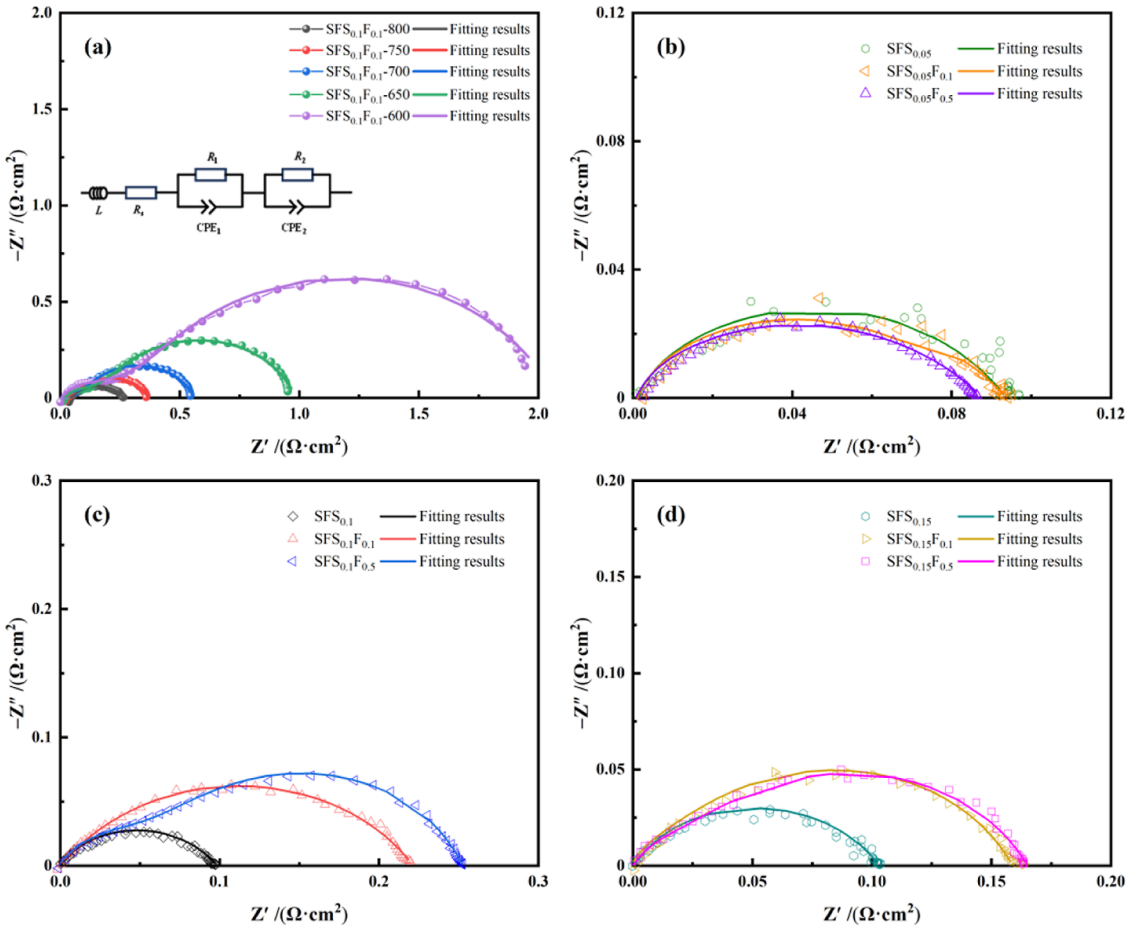

Figure 8. (a) EIS of SFS_xF_y samples at 600−800 °C; (b−d) Nyquist diagram of the symmetrical cell with the SFS_xF_y cathode at 800 °C.

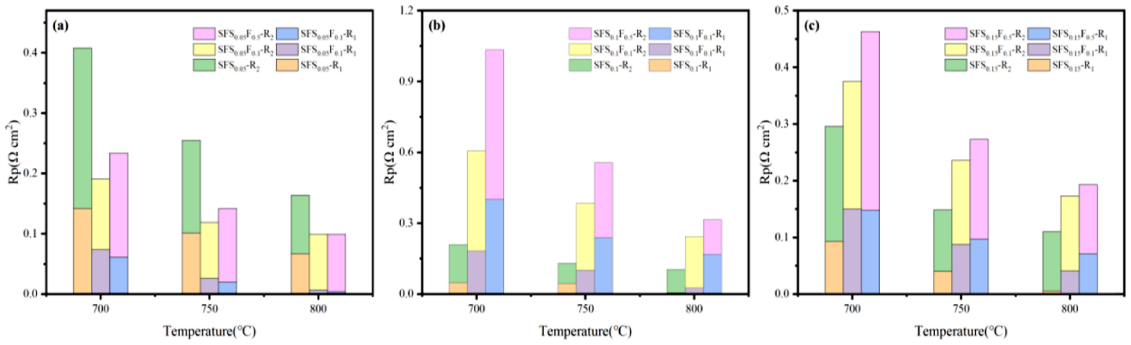

Figure 9. R_p of SF_xSF_y in the range of 700−800 °C.

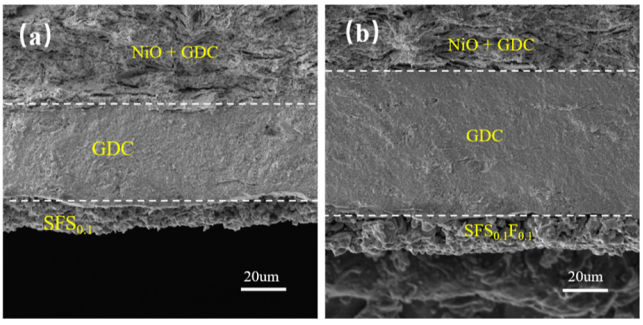

Figure 10. SEM images of the single cell by (a) $SFS_{0.1}$ and (b) $SFS_{0.1}F_{0.1}$ as the cathode.

parameters increased with the increase in the doping amount. $SFS_{0.1}F_{0.1}$ showed good particle distribution and uniform element distribution. The introduction of F increased the CTE of the $SrFe_{1-x}Si_xO_{3-\delta}$ material. When the F doping amount was 0.1, the CTE matched that of common electrolytes. When $SrFe_{0.9}Si_{0.1}O_{3-\delta}$ was doped with F, the ORR activity and conductivity of the $SFS_{0.1}F_{0.1}$ cathode material were improved. The conductivity of the $SFS_{0.1}F_{0.1}$ cathode material reached 170.69 S/cm at 400 °C. At 800 °C, the polarization impedance of $SFS_{0.1}F_{0.1}$ was 0.244 Ω·cm². The double-layer composite cathode with $SrFe_{0.9}Si_{0.1}O_{3-\delta}$ as the cathode material attached well to the GDC electrolyte and had a loose and porous structure, which provided an effective path for oxygen transport and is conducive to cathode ORR. The output

https://doi.org/10.1021/acsomega.4c00869
ACS Omega 2024, 9, 24633−24642

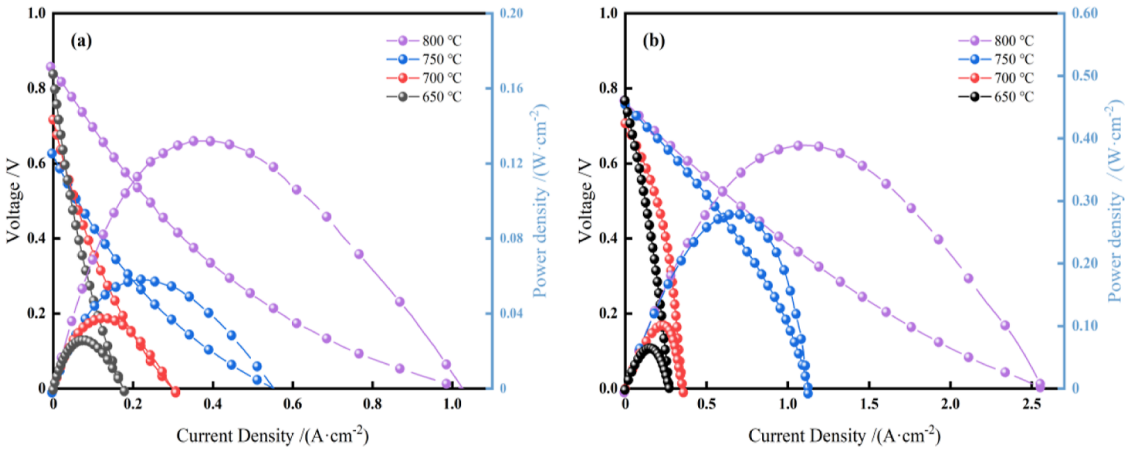

Figure 11. Current density−voltage−power density curves of (a) $SFS_{0.1}$ and (b) $SFS_{0.1}F_{0.1}$.

Table 5. PPD Values of $SrFeO_{3-\delta}$ Materials Doped with Different Elements

sample	electrode	temperature (°C)	PPD (mW cm^{-2})	ref
$SrFe_{0.9}Nb_{0.1}O_{3-\delta}$	SDC	800	407	28
$SrFe_{1-x}Ti_xO_{3-\delta}$ (x = 0−0.15)	SDC	800	475−432	29
$La_{0.8}Sr_{0.2}FeO_{3-\delta}$	SDC	700	300	30
$La_{0.54}Sr_{0.46}Fe_{0.80}Cu_{0.20}O_{3-\delta}$	SDC	600	452	31
$SFS_{0.1}F_{0.1}$	GDC	800	388.91	this work

power density of $SFS_{0.1}F_{0.1}$ as the cathode material reached 388.91 mW/cm^2 at 800 °C. In conclusion, $SrFe_{0.9}Si_{0.1}O_{3-\delta}F_{0.1}$ is a promising cathode material for intermediate-temperature SOFCs.

■ ASSOCIATED CONTENT

Supporting Information

The Supporting Information is available free of charge at https://pubs.acs.org/doi/10.1021/acsomega.4c00869.

EDS image for $SFS_{0.1}$ and $SFS_{0.1}F_{0.1}$, XPS curve of SFS_xF_y: O 1s and Fe 2p, SEM cross-section of dense strip samples for different cathode materials: $SFS_{0.05}$, $SFS_{0.1}$, $SFS_{0.15}$, $SFS_{0.05}F_{0.1}$, $SFS_{0.1}F_{0.1}$, $SFS_{0.15}F_{0.1}$, $SFS_{0.05}F_{0.5}$, $SFS_{0.1}F_{0.5}$, and $SFS_{0.15}F_{0.5}$, surface SEM images of dense strip samples for different cathode materials: $SFS_{0.05}$, $SFS_{0.1}$, $SFS_{0.15}$, $SFS_{0.05}F_{0.1}$, $SFS_{0.1}F_{0.1}$, $SFS_{0.15}F_{0.1}$, $SFS_{0.05}F_{0.5}$, $SFS_{0.1}F_{0.5}$, and $SFS_{0.15}F_{0.5}$, O 1s peak fittings of XPS for SFS_xF_y, and Fe 2p peak fittings of XPS for SFS_xF_y (PDF)

■ AUTHOR INFORMATION

Corresponding Author

Songbo Li − *School of Chemistry and Chemical Engineering, Inner Mongolia University of Science and Technology, Baotou 014010, China*; orcid.org/0000-0001-7603-3042; Email: songboli2021@hotmail.com

Authors

Huipu Ma − *School of Chemistry and Chemical Engineering, Inner Mongolia University of Science and Technology, Baotou 014010, China*

Shengli An − *School of Material and Metallurgy, Inner Mongolia University of Science and Technology, Baotou 014010, China*

Mengxin Li − *School of Chemistry and Chemical Engineering, Inner Mongolia University of Science and Technology, Baotou 014010, China*

Runze Sun − *School of Chemistry and Chemical Engineering, Inner Mongolia University of Science and Technology, Baotou 014010, China*

Qiming Guo − *School of Chemistry and Chemical Engineering, Inner Mongolia University of Science and Technology, Baotou 014010, China*

Complete contact information is available at: https://pubs.acs.org/10.1021/acsomega.4c00869

Notes

The authors declare no competing financial interest.

■ ACKNOWLEDGMENTS

This work was supported by the National Natural Science Foundation of China (No: 51974167), the Scientific Research Program of Inner Mongolia Higher Education Institutions (NJZZ22449), Inner Mongolia Autonomous Region Universities Basic Scientific Research Project 2023CXPT002, Baotou Science and Technology Bureau project YF2022014, and Integrated research platform of novel and important energy comprehensive utilization technology in Inner Mongolia Autonomous Region.

■ REFERENCES

(1) Vinoth Kumar, R.; Khandale, A. P. A review on recent progress and selection of cobalt-based cathode materials for low temperature-solid oxide fuel cells. *Renew. Sustain. Energy Rev.* **2022**, *156*, 111985.

(2) Wang, N.; Huang, Z. Y.; Tang, C. M.; Xing, L. X.; Meng, L.; Aoki, Y.; Du, L.; Ye, S. Y. Functional layer engineering to improve performance of protonic ceramic fuel cells. *Rare Met.* **2023**, *42*, 2250−2260.

(3) Li, Y. H.; Li, Y. P.; Zhang, S. W.; Ren, C.; Jing, Y. F.; Cheng, F. P.; Wu, Q. X.; Lund, P.; Fan, L. D. Mutual Conversion of CO-CO_2 on a Perovskite Fuel Electrode with Endogenous Alloy Nanoparticles for

Reversible Solid Oxide Cells. *ACS Appl. Mater. Interfaces* **2022**, *14*, 9138−9150.
(4) Shah, M. Y.; Lu, Y. Z.; Mushtaq, N.; Singh, M.; Rauf, S.; Yousaf, M.; Zhu, B. ZnO/MgZnO heterostructure membrane with type II band alignment for ceramic fuel cells. *Energy Mater.* **2022**, *2*, 200031.
(5) Mubasher; Mumtaz, M.; Ali, B.; Abbas, S. M.; Nam, K. W.; Khan, M. T.; Ali, M.; Hussain, B.; Khan, M. M.; Mehmood, G. Nanohybrids of hematite nanoparticles and reduced graphene oxide nanosheets: Anode materials for lithium ion batteries. *J. Alloys Compd.* **2022**, *907*, 164392.
(6) Khan, R. U.; Khan, I.; Ali, B.; Muhammad, R.; Samad, A.; Shah, A.; Song, K.; Wang, D. Structural, dielectric, optical, and electrochemical performance of $Li_4Mo_5O_{17}$ for ULTCC applications. *Mater. Res. Bull.* **2023**, *160*, 112142.
(7) Ndubuisi, A.; Abouali, S.; Singh, K.; Thangadurai, V. Recent advances, practical challenges, and perspectives of intermediate temperature solid oxide fuel cell cathodes. *J. Mater. Chem. A* **2022**, *10* (5), 2196−2227.
(8) Singh, M.; Paydar, S.; Singh, A. K.; Singhal, R.; Singh, A.; Singh, M. Recent advancement of solid oxide fuel cells towards semiconductor membrane fuel cells. *Energy Mater.* **2024**, *4*, 4000012.
(9) Merkulov, O. V.; Naumovich, E. N.; Patrakeev, M. V.; Markov, A. A.; Shalaeva, E. V.; Kharton, V. V.; Tsipis, E. V.; Waerenborgh, J. C.; Leonidov, I. A.; Kozhevnikov, V. L. Defect formation, ordering, and transport in $SrFe_{1-x}Si_xO_{3-\delta}$ (x = 0.05−0.20). *J. Solid State Electrochem.* **2018**, *22*, 727−737.
(10) Porras-Vazquez, J. M.; Pike, T.; Hancock, C. A.; Marco, J. F.; Berry, F. J.; Slater, P. R. Investigation into the effect of Si doping on the performance of $SrFeO_{3-\delta}$ SOFC electrode materials. *J. Mater. Chem. A* **2013**, *1*, 11834−11841.
(11) Ivanova, D.; Kovalevsky, A.; Kharton, V. V.; Marques, F. M. B. Efecto de eliminación de sílice en electrolitos sólidos basados en óxido de cerio. *Bol. Soc. Esp. Ceram. Vidrio* **2008**, *47*, 201−206.
(12) Kim, J. S.; Yeon, D. H.; Jung, D. W.; Kwak, C. A highly active and long-term stable La-doped $Ba_xSr_{1-x}Co_{1-y}Fe_yO_{3-\delta}$ cathode for solid-oxide fuel cells. *J. Power Sources* **2014**, *249*, 66−71.
(13) Dai, H. X.; Ng, C.; Au, C. Perovskite-Type Halo-oxide $La_{1-x}Sr_xFeO_{3-\delta}X_\sigma$ (X = F, Cl) Catalysts Selective for the Oxidation of Ethane to Ethene. *J. Catal.* **2000**, *189*, 52−62.
(14) Tarasova, N.; Hanif, M. B.; Janjua, N. K.; Anwar, S.; Motola, M.; Medvedev, D. Fluorine-insertion in solid oxide materials for improving their ionic transport and stability. A brief review. *Adv. Energy Mater.* **2024**, *50*, 104−123.
(15) Oka, D.; Hirose, Y.; Kamisaka, H.; Fukumura, T.; Sasa, K.; Ishii, S.; Matsuzaki, H.; Sato, Y.; Ikuhara, Y.; Hasegawa, T. Possible ferroelectricity in perovskite oxynitride $SrTaO_2N$ epitaxial thin films. *Sci. Rep.* **2014**, *4*, 4987.
(16) Li, F. F.; Liu, D. R.; Gao, G. M.; Xue, B.; Jiang, Y. S. Improved visible-light photocatalytic activity of $NaTaO_3$ with perovskite-like structure via sulfur anion doping. *Appl. Catal., B* **2015**, *166−167*, 104−111.
(17) Ali, B.; Muhammad, R.; Islam, M.; Anang, D. A.; Han, D. S.; Moeez, I.; Chung, K. Y.; Cho, M. K.; Kim, J. Y.; Kim, M. G.; Nam, K. W. Cd-Doped $Li_{4-x}Cd_xTi_5O_{12}$ (x = 0.20) as a High Rate Capable and Stable Anode Material for Lithium-Ion Batteries. *ACS Appl. Energy Mater.* **2023**, *6*, 4198−4210.
(18) Xie, M. Y.; Cai, C. K.; Duan, X. Y.; Xue, K.; Yang, H.; An, S. L. Review on Fe-based double perovskite cathode materials for solid oxide fuel cells. *Energy Mater.* **2024**, *4*, 400007.
(19) Liu, Y. N.; Meng, X. X.; Yu, F. Y.; Yin, M. J.; Yang, N. T.; Meng, B.; Sofianos, M. V.; Liu, S. M. Enhancing oxygen reduction reaction activity of perovskite oxides cathode for solid oxide fuel cells using a novel anion doping strategy. *Int. J. Hydrogen Energy* **2018**, *43*, 12328−12336.
(20) Li, H.; Lu, Z. High-performance fluorine-doped cobalt-free oxide as a potential cathode material for solid oxide fuel cells. *Int. J. Hydrogen Energy* **2021**, *46*, 2503−2510.
(21) Zhang, Z. B.; Zhu, Y. L.; Zhong, Y. J.; Zhou, W.; Shao, Z. P. Anion Doping: A New Strategy for Developing High-Performance Perovskite-Type Cathode Materials of Solid Oxide Fuel Cells. *Adv. Energy Mater.* **2017**, *7*, 1700242.
(22) Hee Kim, J.; Park, Y. I.; Kim, H. A bi-layer cathode based on lanthanum based cobalt- and iron-containing perovskite and gadolinium doped ceria for thin yttria stabilized zirconia electrolyte solid oxide fuel cells. *Ceram. Int.* **2012**, *38* (8), 6303−6310.
(23) Meng, Y.; Zhang, Q.; Chen, Z. J.; Chen, X.; Zhou, J.; Zhu, X. F.; Wang, N.; Zhou, D. F. Novel cobalt and strontium-free perovskite $Pr_{0.5}Ba_{0.5}Fe_{1-x}Ni_xO_{3-\delta}$ (x = 0 and 0.2) as cathode for intermediate-temperature solid oxide fuel cells. *Ionics* **2021**, *27*, 3951−3965.
(24) Bai, J. H.; Han, Z. Y.; Zhou, D. F.; Zhu, X. F.; Wang, N.; Chen, R. Y.; He, J.; Yan, W. F. Preparation of $Pr_2NiO_{4+\delta}$-$La_{0.6}Sr_{0.4}CoO_{3-\delta}$ as a high-performance cathode material for SOFC by an impregnation method. *Int. J. Hydrogen Energy* **2023**, *48*, 6076−6087.
(25) Sun, C. W.; Hui, R.; Roller, J. Cathode materials for solid oxide fuel cells: a review. *J. Solid State Electrochem.* **2010**, *14*, 1125−1144.
(26) Li, H.; Lu, Z. High-performance fluorine-doped cobalt-free oxide as a potential cathode material for solid oxide fuel cells. *Int. J. Hydrogen Energy* **2021**, *46*, 2503−2510.
(27) Moltved, K. A.; Kepp, K. P. The Chemical Bond between Transition Metals and Oxygen: Electronegativity, d-Orbital Effects, and Oxophilicity as Descriptors of Metal-Oxygen Interactions. *J. Phys. Chem. C* **2019**, *20*, 3210−3220.
(28) Zhou, Q. J.; Zhang, L. L.; He, T. M. Cobalt-free cathode material $SrFe_{0.9}Nb_{0.1}O_{3-\delta}$ for intermediate-temperature solid oxide fuel cells. *Electrochem. Commun.* **2010**, *12*, 285−287.
(29) Yu, X. L.; Long, W.; Jin, F. J.; He, T. M. Cobalt-free perovskite cathode materials $SrFe_{1-x}Ti_xO_{3-\delta}$ and performance optimization for intermediate-temperature solid oxide fuel cells. *Electrochim. Acta* **2014**, *123*, 426−434.
(30) Hussain, M.; Muneer, M.; Abbas, G.; Shakir, I.; Iqbal, A.; Javed, M. A.; Iqbal, M.; Zohaib-Ur-Rehman; Raza, R. Cobalt free $La_xSr_{1-x}Fe_{1-y}Cu_yO_{3-\delta}$ (x= 0.54, 0.8, y = 0.2, 0.4) perovskite structured cathode for SOFC. *Ceram. Int.* **2020**, *46*, 18208−18215.
(31) Liu, H. Y.; Zhu, K. Y.; Liu, Y.; Li, W. P.; Cai, L. L.; Zhu, X. F.; Cheng, M. J.; Yang, W. S. Structure and electrochemical properties of cobalt-free perovskite cathode materials for intermediate-temperature solid oxide fuel cells. *Electrochim. Acta* **2018**, *279*, 224−230.

https://doi.org/10.1021/acsomega.4c00869
ACS Omega 2024, 9, 24633−24642